Imaging Ice Sheet Change using Scatterometers

Mark R. Drinkwater[1], David G. Long

October 28, 1997

Abstract

Though designed to measure vector ocean winds, new imaging techniques facilitate the use of spaceborne scatterometer data in climate change studies of polar ice sheets. Contemporary NASA Ku-band Scatterometer (NSCAT) and European Space Agency ERS-1/2 C-band AMI (ESCat), and historical NASA Seasat (SASS) scatterometer data are used to investigate the characteristics of the Greenland and Antarctic ice sheets. Snow and ice 'facies' are clearly delineated on the basis of the radar backscattering cross-section. Comparison of time-dependent scattering characteristics enables change detection, due to sensitivity of radar backscatter to diagenetic changes occurring at and beneath the surface.

Introduction

Recent controversy over the relationship between global warming and changes in the Greenland ice sheet *(1, 2, 3)* make it imperative to measure the current state of mass balance and the timescales of variability in both snow accumulation and ablation. First in 1978 and since 1991, radar-equipped platforms have been employed to understand the relationships between the structure of the snowpack and ice surface and their backscatter characteristics at various frequencies polarizations and incidence angles *(4, 5, 6, 7, 8)*. Satellite radar can be used to map the relative size and locations of ice sheet snow and ice physical zones or 'facies' based on the distinctive scattering signatures of the snow and ice in each zone *(9)*. Backscattering of microwave signals from the surface depends on the roughness and electrical properties which in turn depend on the physical characteristics of the snow and ice cover *(10, 11)*. For example, liquid water in snow dramatically changes its permittivity and thus its

[1]Mark R. Drinkwater[2] is at Jet Propulsion Laboratory, California Institute of Technology, 4800 Oak Grove Dr., Pasadena, CA 91109. David G. Long is at Brigham Young University in the Electrical and Computer Engineering Department, 459 Clyde Building, Provo, UT 84602.

[2]To whom correspondence should be addressed. E-mail: mrd@pacific.jpl.nasa.gov.

microwave scattering signature. This provides an efficient means of monitoring facies changes which are a result of diagenetic changes occurring from melting and snow metamorphosis.

Currently, satellite synthetic aperture radars (SAR) provide high resolution images of ice sheets, but the spatio-temporal coverage of 10OX1OO km scenes is limited. To combat this problem radar mosaics of ice sheets are produced *(12)*. The primary drawback of this technique is that such terrain-corrected digital images take a long time both to acquire and to create. They also do not accurately represent widespread conditions over a sufficiently short period of time to be able to monitor rapid seasonal change. In contrast to SAR, radar scatterometers provide more frequent coverage, albeit at lower resolution. Scatterometers make measurements of the radar backscatter coefficient over a broad range of incidence angles from which the scattering mechanism and signature can be more readily determined. Here we employ data from three scatterometers (SASS, ESCat, and NSCAT) in the study of long-term changes in the Greenland ice sheet.

Scatterometer Imaging

With the recent demise of the Japanese Advanced Earth Observing System (ADEOS I) which carried NSCAT and was launched in August 1996, a valuable tool for ice studies was lost. NSCAT made measurements of the 14 GHz (2.14 cm wavelength) hh- and vv-polarized *normalized radar cross-section* (σ°) of the surface, from which the wind velocity was inferred *(13)*. Measurements were made at various azimuth and incidence angles in hexagonal 25 km resolution cells on a 25 km grid along two 600 km wide swaths separated by a 400 km wide gap. The measurement geometry and timing was selected to optimize NSCAT performance for its primary mission goal of long-term measurement of vector winds over the global oceans. The orbital geometry enabled observation of the polar regions several times each day. The Ku-band SASS, upon which the NSCAT design was based, operated for three months in 1978, making 50 km resolution measurements over two 500 km swaths with an irregular sampling grid *(14)*.

The European Space Agency's ERS-1 and 2 satellites launched in July 1991 and April 1995 [illegible] 5.6 GHz (5.6 cm wavelength) vv-polarized σ° along a single 500 km wide swath *(15)*. ESCat acquires 50 km resolution data on a 25 km grid but is switched off during SAR mode data acquisitions. Over glacial ice, σ° is a function of the measurement incidence angle θ. In the range $\theta \in [20°, 55°]$, σ° (dB) is approximately a linear function of θ, *i.e.*,

$$\sigma^\circ(\theta) = \mathcal{A} + \mathcal{B}(\theta - 40°) \qquad (1)$$

where the coefficients $\mathcal{A}$ and $\mathcal{B}$ depend on surface characteristics, polarization, and

azimuth angle. $\mathcal{A}$ is the 40° "incidence angle-normalized" σ^o value, while $\mathcal{B}$ describes the dependence of σ^o on θ. $\mathcal{A}$ and $\mathcal{B}$ provide useful descriptors of the sensitivity to snow and ice surface characteristics.

We use the scatterometer image reconstruction algorithm with filtering (SIRF) to generate enhanced resolution images of $\mathcal{A}$ and $\mathcal{B}$ from the scatterometer measurements. SIRF was originally developed for SASS data (16) and has been previously applied to Greenland *(9)*. A modified form of SIRF is used for EScat and has been used for Antarctic sea-ice studies *(17)*. SIRF uses multiple, overlapping measurements of σ^o and post-processing to improve the resolution of the A and $\mathcal{B}$ images (18). Multiple passes are required to achieve the required overlap. Over land targets, $\mathcal{A}$ and $\mathcal{B}$ are assumed to remain relatively constant over the imaging; time interval, at least for sufficiently short intervals. In the polar regions a minimum of 6 days is required to obtain reasonable images, though better images are obtained with longer time periods. The resulting 6-day images are therefore a trade-off between resolution enhancement and temporal averaging.

Mapping Ice Sheet Facies and Interannual Variability

The surface of the Greenland ice sheet may be subdivided into zones or 'facies' a variety of types within whose near-surface geophysical properties have unique characteristics *(19)*. Boundaries between these facies are established with respect to the time at which maximum melt conditions prevail. At the lowest elevations, summer melting removes the entire annual accumulation of snow to reveal bare glacier ice. The *firn line* delimits the upper margin of this zone, separating it from the 'soaked' facies where complete saturation of the annual snow layer occurs. The upper limit of soaking is called the *saturation line*. Localized melt-water percolation occurs between this and the upper limit of surface melting, the *dry-snow line*. In the percolation facies the annual increment of snow is neither completely wetted nor raised to the melting point. Percolation decreases with elevation diminishing to a negligible amount at the lower boundary of the dry snow zone.

Using optical satellite data it was concluded that visible wavelengths are inappropriate for routine mapping of boundaries between facies because these are not [illegible] *(19)*. The glacier facies are best discerned with measurements penetrating several meters into the surface of the snow and ice. Microwaves are suited for such observations since they are particularly sensitive to variations in both surface and subsurface characteristics *(8, 10, 11, 21)*.

Seasonal modulations of σ^o in 1978 SASS and 1992 EScat data shown in Figure 1 are a demonstration of the sensitivity to spatio-temporal transitions in surface and subsurface properties. The principal parameter affecting the microwave response of the ice sheet is the seasonal presence of melt water in areas experiencing summer melt. After liquid water, σ^o is primarily affected by the layering developing as a

consequence of seasonal snow accumulation and melt patterns. Changes in the snow caused by melting can result in reductions in σ^o exceeding 15 decibels*(9)*. Meltwater changes the dielectric properties of snow and ice so significantly that it regulates the reflection or transmissivity at the surface and limits subsurface volume scattering effects by increasing absorption and extinction within the upper layers*(22)*. In Figure 1 the spatial extent of summer melt is captured and highlighted as extremely low σ^o values (black), particularly on day 209 at the beginning of the time series. Since the response to surface melt is similar at C- and Ku-band, differences in melt extent between the upper and lower panels are accounted for by interannual variability in the length and spatial extent of the melt seasons. Surface melting extends along the entire western flank of the ice sheet between days 209 - 214 in 1978, whereas in 1992 the surface appears to have either already frozen or experienced less melting. Typically, by late August (day 237) melting ceases, and refreezing of the surface layer increases the values of σ^o at both frequencies.

In Figure 2 pixels experiencing melt are mapped in summer C-band ESCAT images for the years 1992-1997. An algorithm is applied which tracks melting in the images as a function of the sharp reduction in backscatter during mid-July. Resulting monthly average images of July melt extent are shown together with a Figure 2a 1996 map indicating the primary snow and ice zones recovered in conjunction with Ku-band NSCAT image data. Results shown in Figure 2 indicate that during the 1990's the Greenland ice sheet has experienced two of the smallest (1992: $8.1 \cdot 10^4$ sq km; and 1996: $10.4 \cdot 10^4$ sq km), and perhaps the largest (1995: $25 \cdot 10^4$ sq km) melt extent in the last two decades. In 1995 melting is significantly more extensive than at any other time during the satellite data record *(3)*, encroaching upslope upon the dry snow zone along the entire north-western flank of the ice sheet.

In the percolation zone, stratigraphic discontinuities forming from seasonal ablation or metamorphosis are generally preserved over time until carried downslope by ice velocity). A distinct horizon forms comprising a high proportion of solid ice in layers, lenses and ice pipes. This is created as meltwater percolates downwards and refreezes at depth (~1 m) in the relatively colder snow *(19)*. The lower boundary of this zone is clearly indicated in Figure 1 by a sharp transition between low and extremely high backscatter values caused by buried scatterers. As the surface layers cool

highest known values of backscatter on earth, in both Ku and C-band images *(10, 11)*. This characteristic of the dual-frequency backscattering was used to derive the lower boundary in the snow facies map in Figure 2.

During autumnal cooling, as the active surface layer refreezes and snowfall takes place, microwaves penetrate to increasing depths. This enables distinction between the dry snow regime at the highest elevations of the ice sheet, and the percolation facies downslope of the maximum melt extent (*i.e.* 'dry snow line'). The dry snow

zone, experiences negligible backscatter change from one year to the next, since by definition it is the region experiencing little or no surface melting during summer. Due to rapid grain growth and the formation of ice layers and lenses in the percolation zone, a sharp spatial gradient in backscatter delimits the two zones during autumn. By the end of the Figure 1 time series, low backscatter returns at high altitude (in central Greenland) are well delineated from percolation zone values exceeding -5 dB. In dry snow, C-band microwaves penetrate somewhat more effectively than Ku-band with relatively smaller absorption scattering and absorption losses. At Ku-band microwaves are more effectively scattered, particularly by snow grains. Thus Ku-band snow volume scattering is greater than at C-band in the dry snow zone. In contrast, in the percolation zone, ~~-bane] penetrates more effectively to sense buried scatterers. q'bus, a frequency ratio $\mathcal{A}$ image (*i.e.* ESCat - NSCAT) is used to contour the locations at which this contrast reversal is observed. The result is shown in Figure 2 (a).

Downslope of the firn line, in the saturated facies, horizons tend to be obliterated by the effects of summer melting. This likely reduces tile contrast between the ablation and saturated zones. As a result these two zones are indistinguishable from one another on the basis of the winter backscatter, and radar senses only a broad 'ablation zone' *(9)*. Differences in physical properties between the percolation zone and ablation zone are sufficient to cause large differences in snow backscattering after fall-freezeup has taken place. The hard ice surface (or iced firn) in the ablation zone, has a different appearance from firn upslope. Furthermore, there are no buried scatterers or layers to produce volume scattering. Near tilt' ice sheet margins, surface penetration of microwaves of either wet snow, firn or ice is negligible with the shape of the surface roughness autocorrelation function being the most important determinant of σ^o and hence $\mathcal{A}$ and $\mathcal{B}$ via surface scattering. The scale of surface roughness of the summer surface in the ablation zone results in significantly greater backscattering at smaller wavelengths, with Ku-band surface backscattering at 40° incidence exceeding ('-hand surface scattering by 10 dB or more in the south-western ablation zone shown in Figure 2 and Figure 3. This attribute together with the seasonal variation in σ^o are used to define the 1996 extent of the ablation zone in Figure 2a.

Long-term Changes in the Greenland Ice Sheet

The real potential of consecutive, similar scatterometer missions is the likelihood of obtaining repeat image data which can be employed in detecting long-term changes in the large ice sheets. Recent acquisition of NSCAT data over the Greenland ice sheet, during the same period of the year as Seasat, enables long-term (18 year) change maps to be derived, by calculating the difference in σ^o (*i.e.* NSCAT-SASS) between seasonal mean images from the period after autumnal cooling. Figure 3a shows the vv-polarized NSCAT image for the period between day 267 and 272 (24 - 29 Sept.) in

1996. Alongside in Figure 3b is the result of combining and median filtering the sparse measurements obtained by SASS between days 250 and 283 (6 Sept. - 9 Oct.) in 1978. The result in each case is a seasonal average image for the period following the autumnal freeze-up and following progression of the zero degree isotherm downslope beyond the percolation zone. Figure 3b is essentially similar in image characteristics to Figure 1 d. Subtle differences between the NSCAT and Seasat SASS A images are shown in Figure 3c, with differences highlighted for the range ± 3 dB. Surfaces experiencing extreme changes are noted as either dark or light tones. Black indicates a reduction in backscatter of -3 dB or more over the 18 year period, while light tones show regions with > 3 dB of increase.

The Ku-band A difference image in Figure 3c is the difference between two seasonal snapshot images and contains a record of the zones of greatest variability in σ^o over the intervening 18 year period, through the impact of snow stratigraphy changes. Patterns in Figure 3c indicate a spatial pattern highly correlated with the snow and ice facies identified in Figure 2a *(19)*. Figure 3c essentially illustrates the areas of primary interannual variability within each of the respective snow and ice facies. It indicates is that the melt line (*i.e.* lower boundary of dry-snow zone) has an extremely large interannual variability, not previously identified in radar data. Figure 2 indicates large changes in the mean melt area, but the July monthly mean does not capture the maximum extent of melting often only experienced within a narrow range of dates. Normally this occurs around mid July with typical interannual variability of several days in the timing of peak melt.

The A difference image in Figure 3c contains microwave archaeological radar evidence for previous melting within the dry snow zone, through the influence of buried scatterers beneath the most recent year's annual snow accumulation. Evidence suggests a recent upslope migration of the upper boundary of the percolation zone. From Figure 2c, and evidence in Figure 3c 1995 appears to have experienced the maximum melt extent within the last two decades. This conclusion is made because NSCAT penetrates sufficiently deeply to sense percolation inhomogeneities produced in the summer of 1995 along the lower elevation fringes of the dry snow zone. A frequency difference A image (ΔA = NSCAT-ESCAT) in Figure 3d corroborates changes observed in 3c. It shows the difference in σ^o between the Ku- and C-band A images

[illegible] dry snow zone, due to the primary [illegible] originating from snow grain Rayleigh scattering. In the absence of strong stratigraphy, the dry snow zone produces large positive values in Figure 3c. Neutral values occur in the zone influenced by percolation, due to both wavelengths responding to buried inhomogeneities. Downslope in the ablation zone, positive values return likely due to the small scale roughness.

Recently, dry snow zone accumulation (Q) rates *(23)* were compared with C-band A and B pixel values in non-enhanced 50 km resolution ERS-1/2 images *(24)*.

Results indicated a favorable 79% correlation coefficient for the following exponential relationship:

$$ln(Q) = 7.21|\mathcal{B}| + 4.0 \quad (2)$$

although a large standard deviation of $67\,kgm^{-2}a^{-1}$. Improvements in the spatial resolution were demonstrated to improve this correlation particularly in regions where the spatial gradients in Q are as high as $200kgm^{-2}a^{-1}$ per 25 km such as the dry snow zone on the western frank of the ice sheet.

The relationship in (2) implies that lower accumulation rates result in more pronounced stratification, and more efficient backscattering from subsurface layers at high incidence angles. This is particularly true for instance in the north-east dry snow zone, and is demonstrated in SASS data *(9)*. Thus we suggest that time- series of multiple frequency enhanced resolution $\mathcal{A}$ images (such as Figure 3d) and their associated $\mathcal{B}$ values. offer better possibilities for retrieving snow accumulation than single channel, fixed incidence angle instrument data. Frequency combinations and tile addition of passive microwave emission data from SSM/I will help compensate for the wavelength- dependent scattering albedo of the snow and the high incidence angle component of volume backscatter caused by snow grains, as opposed to the stratification induced scattering. This will allow dependencies of the backscattering on snow density, temperature, ice particle radius and layer depth to be better parameterized. In this manner, algorithms may be developed to monitor the seasonal progression of snow accumulation and firnification.

Conclusion]]

Scatterometers clearly provide important information about the large ice sheets such as Greenland. This spatial and temporal information is complementary to higher resolution sensors such as SAR, and passive microwave images from SSM/I.

Time series of images with large-area coverage, such as the radar scatterometer images shown here, are therefore suitable for monitoring changes in the characteristic zones of ice sheets in response to changes in accumulation and melting. The significant 18 year difference between early NSCAT images collected in September 1996, and Seasat SASS images collected in 1978 indicates large-scale changes in the radar backscattering in response to changing snow and ice surface conditions. The central dry snow zone provides a stable reference signature over the 18 year interval since Seasat, while changes in the bordering zone imply an upslope increase in the extent of the percolation zone. This implies that the region of melting on the ice sheet has risen to its highest altitude in the recent past. Observations of the interannual variability suggest that 1995 was an extremely high melt year, probably the highest since 1978 Seasat observations.

Data such as this may be used to chart significant changes in the locations of

the primary boundaries between snow facies in response to adjustments in the mass balance of the ice sheet. Our results suggest a methodology which may be used to consistently recover the areas affected by seasonal melting, such that snow and ice facies may be temporally monitored by radar satellite. In this manner the response of large ice sheets to climate changes may be effectively monitored.

References AND NOTES

1. H.J.Zwally, A.C.Brenner, *Science*, 246, 15 S7-1.591 (19S9).

2. W.L. Chapman, J.E. Walsh, *Bull. Am. Met. Soc.*, **74**(1), 33-47. (1993).

3. W.Abdelati. K. Steffen, *J. Climate*, **10**(2), 165-175. (1997).

4. C. Elachi and W.E. Brown, *J. Geophys. Res.* **80**. 1113-1119 (1975)

5. H. Rott, *Z. fuer Gletscherkunde u. Glazialgeol.*, **16**. 255-266 (1980)

6. M.R. Drinkwater, J.A. Dowdeswell, *Ann. Glaciology*. **9**, 60-68 (1987).

7. Rott, H., K. Sturm, H. Miller, *Annals of Glaciol.*, **17**, 337-343 (1993).

8. Jezek. K.C., M.R. Drinkwater, J.P. Crawford, R. Bindschadler, R. Kwok, *J. Glaciology*. **39**, 131, 119-132 (1993).

9. D.G. Long, M.R. Drinkwater, *J. Glaciology*, **32**, 2, 213-230 (1991).

10. E. Rignot, *J. Geophys. Res.*, **100**, E5, 9389-9400 (1995).

11. Jezek, K.C., P. Gogineni, M. Shanableh, *Geophys. Res. Lett.*, **21**, 1, 33-36 (1994).

12. M. Fahnestock, R. Bindschadler, R. Kwok, K. Jezek, *Science*, **262**, 1530-1534, (1993).

13. F. Naderi, M.H. Freilich, D.G. Long, *Proc. IEEE*, **79**, 6, 850-866 (1991).

14. W.J. Jones, J.C. Sciremmer, E.M. Bracalente, R.A. Brown, G.J. Dome, W.J. Pierson, and F.J. Wentz, *J. Geophys. Res.*, **87**(C5), 3297-3317 (1982).

15. E.P. Attema, *Proc. IEEE*, **79**, 791-799 (1991).

16. D.G. Long, P.J. Hardin, P.T. Whiting, *IEEE Trans. Geosci. Rem. Sens.*, **31**, 3, 700-715 (1993).

17. M.R. Drinkwater, D.G. Long, D.S. Early, *ESA Journal* **17**, 307-322 (1991).

1 S. 1). S. Early, D.G. Long, Resolution Enhancement of Scatterometer Data, *IEEE Trans. Geosci. Rem. Sens.*, In Press. (1 997).

19. C.S. Benson, Cold Reg. *Res. Eng. Lab. Rep.*, 10, *(1962)*.

20. R.S. Williams Jr., D.K. Hall, and C.S. Benson, *J. Glaciol.*, **37**, 120-12s (199]).

21. C.T. Swift, P.S. Hayes, J.S. Herd, W.L. Jones, V.E. Delnore, *J. Geophys. Res.*, 90, 132, 19s3-1994 (19s5).

22. C. Maetzler, *Rem. Sens. Rev.*, 2, 259-387 *(19S7)*.

23. A. Ohmura and N. Reeh, *J. Glaciol.*, 37(125), 140-14S (1991).

24. P. Gudmandsen, *personal communication*, (1997).

25. We thank XXX and XXX for reviewing the manuscript and Gardner Watt, Quinn Remund and David Early for their assistance in preparing the figures. MRD completed this work at Jet Propulsion Laboratory, California institute of Technology under contract, to the National Aeronautics and Space Administratier}. This work was supported by R.H. Thomas of NASA's Mission to Planet Earth Office.

Figure Captions

Figure 1. Greenland time series images generated from 1978 Ku-band SASS data and 1992 C-band ERS-1 data using the resolution enhancement technique. Image data are derived for the Julian day periods indicated. Colors indicate the incidence-angle normalized backscattering coefficient for each frequency at a mid-swath angle of 40°.

Figure 2. (a) Greenland snow and ice facies determined from 1996 EScat and NSCAT data; and (b)-(f) mean monthly ice sheet melt extent, determined from E.Scat scatterometer images from 1992 to 1996.

Figure 3. (a) NSCAT *A* image for the period 267-272, 1996; (b) SASS *A* image for days 2,50 -283,1978; (c) NSCAT – SASS $\mathcal{A}$ difference map of Greenland. (d) ERS-2 $\mathcal{A}$ image for days 267-272. 1996; and (e) ERS – NSCAT (C – Ku band) *A* difference image for days 267-272.

Cover **Caption**

A 14.6 GHz, incidence-angle normalized radar backscatter image of Antarctica and the surrounding sea-ice cover, showing variations in the snow conditions due to accumulation, melting, and surface roughness. This is the first-ever single Ku-band radar image image of the entire Antarctic ice sheet, and was made from six days of consecutive orbital swath data from the NASA Scatterometer (NSCAT) with the aid of a resolution-enhancement algorithm. These data present a new ice-sheet monitoring application of the NSCAT instrument aboard the ADEOS-I spacecraft, which was originally designed to measure near-surface wind velocities over the ice-free ocean. See article on page XXXX by Drinkwater and Long. [Image: David Long and Mark Drinkwater - data courtesy of JPL and NASDA].

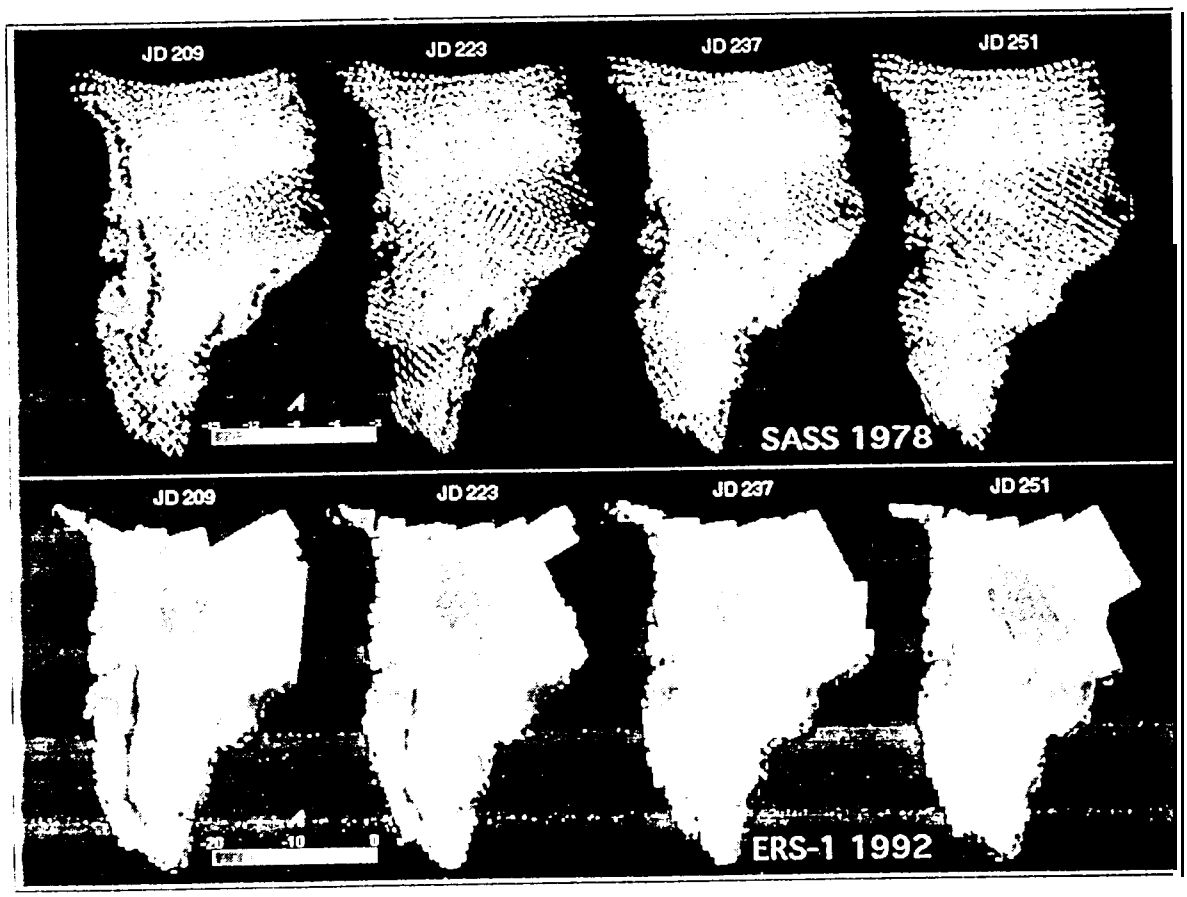

Figure [illegible] Ku-band SASS data and [illegible] are derived [illegible] normalized

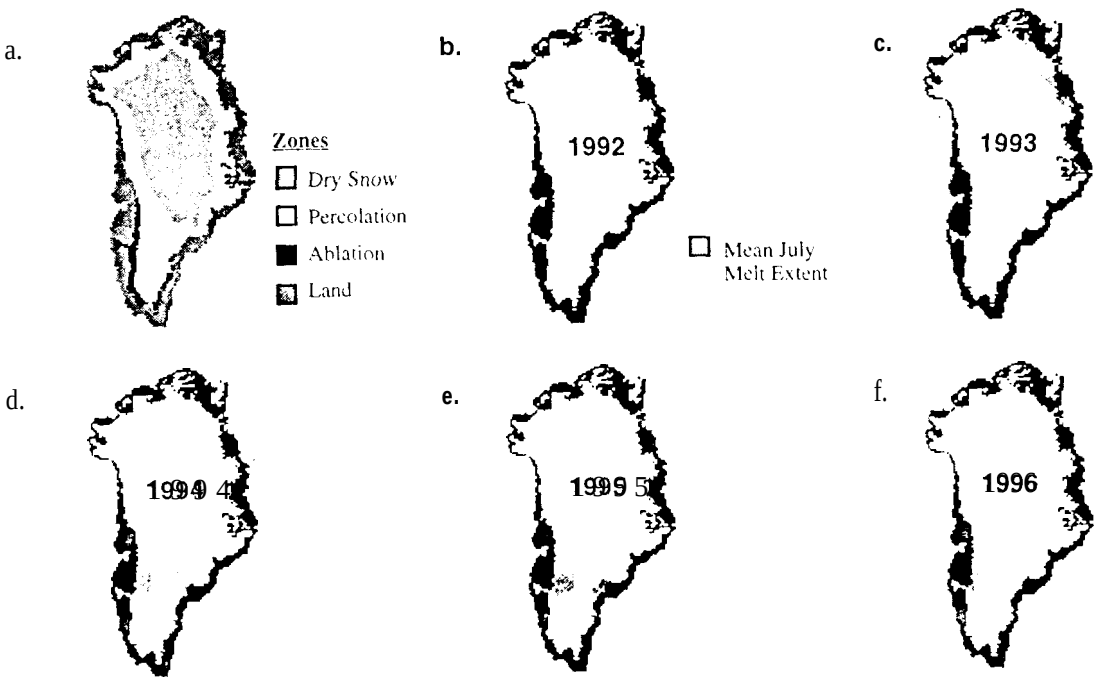

Figure 2. (**a**) Greenland snow and ice zones; (**b**)-(**f**) mean monthly ice sheet melt extent, determined from ERS-1/2 and NSCAT scatterometer images from 1992 to 1996.

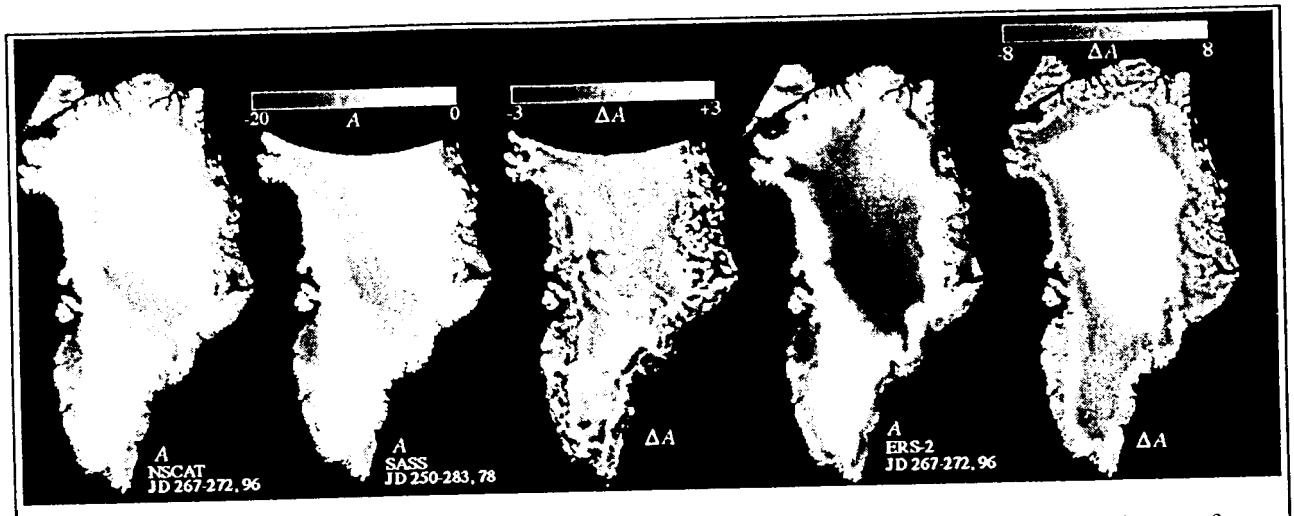

Figure 3. (a) Greenland NSCAT *A* image for the period 267-272, 1996; (b) SASS *A* image for days 250-283, 1978; (c) 18-year NSCAT-SASS *A* difference image; (d) ERS-2 *A* image for days 262-272, 1996; (e) ERS - NSCAT (C - Ku band) *A* difference image.

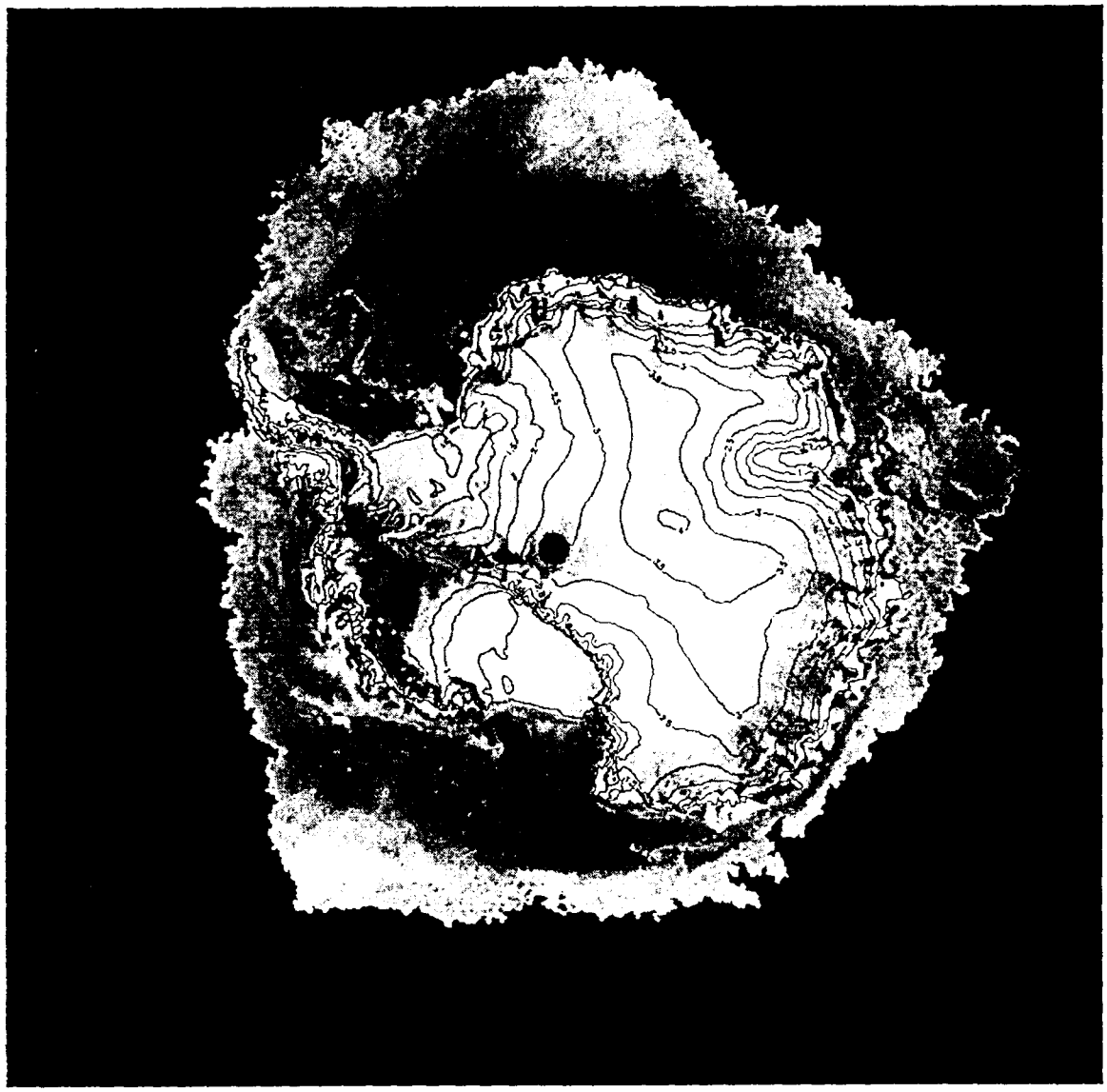

Cover Caption

A 14-GHz incidence-angle normalized, radar backscatter image of Antarctica and the surrounding sea-ice cover, showing variations in the snow conditions due to accumulation, melting, and surface roughness. This is the first-ever single Ku-band radar image of the entire Antarctic ice sheet, and was made from six days of consecutive orbital swath data from the NASA Scatterometer (NSCAT) with the aid of a resolution-enhancement algorithm. These data present a new ice-sheet monitoring application of the NSCAT instrument aboard the ADEOS-I spacecraft, which was originally designed to measure near-surface wind velocities over the ice-free ocean. See article on pages ???-??? by Drinkwater and Long. [Image: David Long and Mark Drinkwater - data courtesy of JPL and NASDA].